Research Article | Vol. 26, No. 15 | 23 Jul 2018 | OPTICS EXPRESS 19665
Optics EXPRESS

Mechanism of single-shot damage of Ru thin films irradiated by femtosecond extreme UV free-electron laser

IGOR MILOV,[1,*] IGOR A. MAKHOTKIN,[1] RYSZARD SOBIERAJSKI,[2] NIKITA MEDVEDEV,[3,4] VLADIMIR LIPP,[5] JAROMIR CHALUPSKÝ,[3] JACOBUS M. STURM,[1] KAI TIEDTKE,[6] GOSSE DE VRIES,[7] MICHAEL STÖRMER,[8] FRANK SIEWERT,[9] ROBBERT VAN DE KRUIJS,[1] ERIC LOUIS,[1] IWANNA JACYNA,[2] MAREK JUREK,[2] LIBOR JUHA,[3,4] VĚRA HÁJKOVÁ,[3] VOJTĚCH VOZDA,[3,10] TOMÁŠ BURIAN,[3,4,11] KAREL SAKSL,[12] BART FAATZ,[6] BARBARA KEITEL,[6] ELKE PLÖNJES,[6] SIEGFRIED SCHREIBER,[6] SVEN TOLEIKIS,[6] ROLF LOCH,[6] MARTIN HERMANN,[13] SEBASTIAN STROBEL,[13] HAN-KWANG NIENHUYS,[7] GRZEGORZ GWALT,[9] TOBIAS MEY,[14] HARTMUT ENKISCH,[13] AND FRED BIJKERK[1]

[1]*Industrial Focus Group XUV Optics, MESA+ Institute for Nanotechnology, University of Twente, Drienerlolaan 5, 7522 NB Enschede, The Netherlands*
[2]*Institute of Physics Polish Academy of Sciences, Al. Lotników 32/46, PL-02-668 Warsaw, Poland*
[3]*Institute of Physics, Czech Academy of Sciences, Na Slovance 2, 182 21 Prague 8, Czech Republic*
[4]*Institute of Plasma Physics, Czech Academy of Sciences, Za Slovankou 3, 182 00 Prague 8, Czech Republic*
[5]*Center for Free-Electron Laser Science CFEL, Deutsches Elektronen-Synchrotron DESY, Notkestrasse 85, Hamburg 22607, Germany*
[6]*Deutsches Elektronen-Synchrotron DESY, Notkestrasse 85, Hamburg 22607, Germany*
[7]*ASML Netherlands BV, PO Box 324, Veldhoven, 5500 AH, The Netherlands*
[8]*Helmholtz-Zentrum Geesthacht, Max-Planck-Strasse 1, Geesthacht 21502, Germany*
[9]*Helmholtz Zentrum Berlin für Materialien und Energie, Albert-Einstein-Strasse 15, Berlin 12489, Germany*
[10]*Institute of Physics, Faculty of Mathematics and Physics, Charles University in Prague, Ke Karlovu 5, 121 16 Prague 2, Czech Republic*
[11]*J. Heyrovský Institute of Physical Chemistry, Czech Academy of Sciences, Dolejškova 2155/3, 182 23 Prague 8, Czech Republic*
[12]*Institute of Materials Research, Slovak Academy of Sciences, Watsonova 47, 040 01 Košice, Slovak Republic; Faculty of Science, Institute of Physics, Pavol Jozef Šafárik University in Košice, Košice 041 80, Slovakia*
[13]*Carl Zeiss SMT GmbH, Rudolf-Eber-Strasse 2, Oberkochen 73447, Germany*
[14]*Laser-Laboratorium Göttingen eV, Hans-Adolf-Krebs-Weg 1, Göttingen 37077, Germany*
[*]*i.milov@utwente.nl*

Abstract: Ruthenium is a perspective material to be used for XUV mirrors at free-electron laser facilities. Yet, it is still poorly studied in the context of ultrafast laser-matter interaction. In this work, we present single-shot damage studies of thin Ru films irradiated by femtosecond XUV free-electron laser pulses at FLASH. *Ex-situ* analysis of the damaged spots, performed by different types of microscopy, shows that the weakest detected damage is surface roughening. For higher fluences we observe ablation of Ru. Combined simulations using Monte-Carlo code XCASCADE(3D) and the two-temperature model reveal that the damage mechanism is photomechanical spallation, similar to the case of irradiating the target with optical lasers. The analogy with the optical damage studies enables us to explain the observed damage morphologies.

#331377 https://doi.org/10.1364/OE.26.019665
Journal © 2018 Received 10 May 2018; revised 28 Jun 2018; accepted 10 Jul 2018; published 20 Jul 2018

Optics EXPRESS

1. Introduction

Radiation parameters of extreme ultraviolet (XUV) free-electron laser (FEL) light sources such as FLASH [1] or FERMI [2] create challenges for the optical elements operating at such facilities. High-peak power femtosecond pulses generated by FELs induce ultrafast and highly non-equilibrium processes in the irradiated material. Such processes may lead to degradation and significant damage of the material, strongly reducing its optical performance. In order to prevent optics from being damaged and, thus, to increase its lifetime, fundamental understanding of the nature of XUV laser-induced damage formation is required.

Previous studies of XUV-induced damage focused on various materials that are of interest for XUV optics. Mo/Si-based multilayers are commonly used as normal incidence mirrors optimized for a wavelength of 13.5 nm. Thermally-induced compaction of the multilayer due to energetically stable silicide formation was found to be the leading damage mechanism for both nanosecond pulses generated with a table-top laser produced plasma (LPP) source [3] and femtosecond pulses at FLASH [4], with the latter damage threshold being several factors lower than in the ns case. In order to increase the damage threshold value, Mo/Si multilayers with different capping layers [5, 6], diffusion barriers [5] or thermodynamically stable compounds [7] were also considered.

Other materials used in XUV optics as grazing incidence mirrors are metal or carbon-based films that work on the principle of total external reflection. For B_4C and SiC samples it was found that the damage threshold strongly depends on the photon energy. In the range of 38 - 830 eV it was typically of the order of the fluence required for thermal melting [8–10]. Another damage mechanism, namely solid-solid phase transition (graphitization), was reported when irradiating a-C samples with femtosecond pulses with 91.8 and 177.1 eV photon energies [11, 12]. For gold films surface melting with subsequent complete removal of the film was observed when exposed to XUV light from an LPP source [3]. Similar damage morphologies showing a step-like complete removal of the gold film were reported for a femtosecond pulse case [13].

Ablation of metals with optical lasers was extensively studied in the literature [14–18]. However, the interaction of XUV light with metals is fundamentally different. The photons with higher energy can create strongly non-equilibrium states of the electronic system and also excite deep shells of target atoms, not only the conduction band. Additionally, since in our experiments grazing incidence conditions are applied, the energy is absorbed in a very thin (few nanometers) layer. This may result in realization of more extreme conditions in the material compared to the excitation with optical lasers having the same amount of absorbed energy. In this work, we investigate whether these differences have a significant impact on the single-shot damage process.

We study the nature of single-shot damage induced in ruthenium (Ru) thin films by femtosecond XUV pulses generated by FLASH. Ru is chosen as optically favorable material, since it has a high XUV reflectance in a wide range of grazing incidence angles [19] and is relatively resistant to oxidation [20]. Ru is also a standard material for grazing incidence hard X-ray optics [21].

In order to understand the mechanisms responsible for the observed damage, we perform simulations of the interaction of femtosecond XUV laser pulses with the Ru target. Generally for metals, such interaction proceeds in three characteristic stages. (i) The absorption of XUV photons induces non-equilibrium electron kinetics in the near surface region of the metal. During that stage, photo- and secondary electrons travel ballistically with velocities high above the Fermi velocity. After several collisions these electrons thermalize to a Fermi-Dirac distribution with an elevated electron temperature, while the lattice remains cold. (ii) The second stage is characterized by thermal non-equilibrium between electrons and the lattice. During that stage thermalized electrons diffuse into the depth of the metal, while simultaneously heating up the lattice via electron-phonon interaction, until electron and lattice temperatures are equal. (iii) Equilibrium thermal diffusion proceeds in the third stage. When the laser pulse fluence is sufficiently high, various damage processes such as melting and resolidification, mechanical

Optics EXPRESS

fracture or phase explosion may occur after the interaction with the laser pulse [17].

In the present work, apart from the experimental study, we use a combined computational approach to describe the interaction of XUV FEL femtosecond pulses with a Ru film. The first stage mentioned above, non-equilibrium electron kinetics induced by XUV light, is simulated with the classical Monte Carlo code XCASCADE(3D) [22]. The code models the absorption of XUV photons by the target and follows the temporal and spatial evolution of the electron cascades produced upon photoabsorption.

The second and third stages are described using the two-temperature model (TTM) [23]. Typically, the TTM is used to simulate the interaction of optical lasers with solids [14, 15, 24–27]. It assumes that the electronic system is always in thermal equilibrium, so it can be described with a temperature. Contrarily to visible light, XUV photons have sufficient energy to ionize core shells of the target atoms, creating highly non-equilibrium electronic states, which is not possible to describe with the TTM alone.

For that reason, the XCASCADE(3D) calculations are performed prior to the TTM, so that XUV-induced non-equilibrium electron kinetics is taken into account. Coupling of the two models is realized in the following way: the transient energy density depth profiles of thermalized electrons obtained from XCASCADE(3D) are used to calculate the heat source term for the TTM.

Our calculations give detailed information about the ultrafast heating of the Ru lattice, which is of crucial importance for understanding the mechanisms responsible for the observed damage phenomena.

2. Experiment

We performed single-shot damage experiments with Ru thin films at FLASH. The FEL in the configuration used in the experiment provided single pulses of 100 fs duration (FWHM) at 13.5 nm wavelength (92 eV photon energy) with 1% spectral bandwidth. The FEL beam was p-polarized with respect to the sample surface and focused using a carbon coated ellipsoidal mirror. The experiment was performed in a high vacuum experimental chamber with a base pressure better than 10^{-6} mbar. The samples, clamped on a sample holder that was controlled by a motorized manipulator, were exposed to FEL radiation at 20° grazing incidence angle. For each single shot pristine material was exposed. Sample position monitoring and *in-situ* investigation of strongly damaged spots were performed using an optical microscope mounted onto the vacuum chamber. The energy of each pulse was attenuated with gas and/or solid attenuators with calibrated transmission factors and was measured with a gas monitor detector [28]. The energy range of $0.2 - 46$ μJ per pulse was chosen so that the highest values create heavily damaged surfaces, while for the lowest values no damage was observed by means of the *in-situ* optical microscope. More details about the experimental set-up and procedures can be found elsewhere [19, 29].

The spatial energy distribution of FEL beams is typically non-Gaussian. Therefore, the beam profile should be characterized prior to laser-matter interaction experiments. The fluence scan method [30, 31], based on single-shot ablative imprints on PMMA, was used to measure the effective area of the beam, A_{eff}. In this experiment A_{eff} was measured to be 41 μm^2 in the normal incidence condition, which corresponds to 120 μm^2 at 20° grazing incidence. The peak fluence F of each pulse can be calculated from the pulse energy E_p, which is directly measured in the experiment, and the effective area A_{eff} as $F = E_p/A_{eff}$. The total error for the peak fluence determination is estimated to be $\sim 20\%$. This value represents a combined error of pulse energy measurements and determination of the effective area of the beam.

A ruthenium polycrystalline metal film of 50 nm thickness was used as a target. The sample was prepared by depositing ruthenium on a naturally oxidized superpolished silicon substrate using the magnetron sputtering technique. The thickness of the film was determined with X-ray reflectivity measurements.

Optics EXPRESS

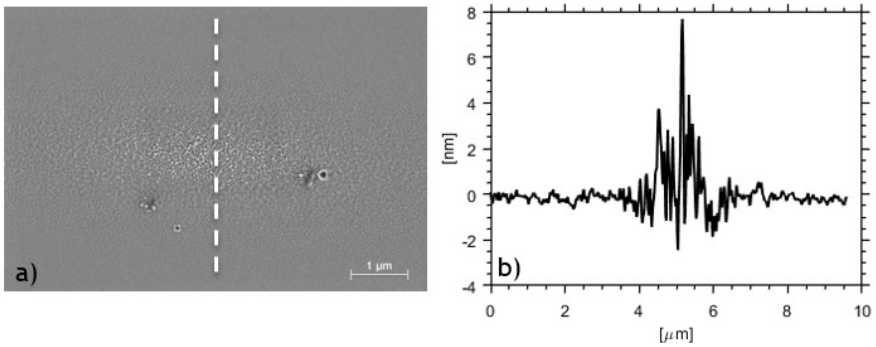

Fig. 1. (a) HR-SEM image of the damaged spot produced by the 100 fs XUV FEL pulse with an incident peak fluence of $F = 213$ mJ/cm^2. The dashed vertical line indicates where the AFM line profile is made. (b) Line profile in the center of the spot extracted from the AFM scan.

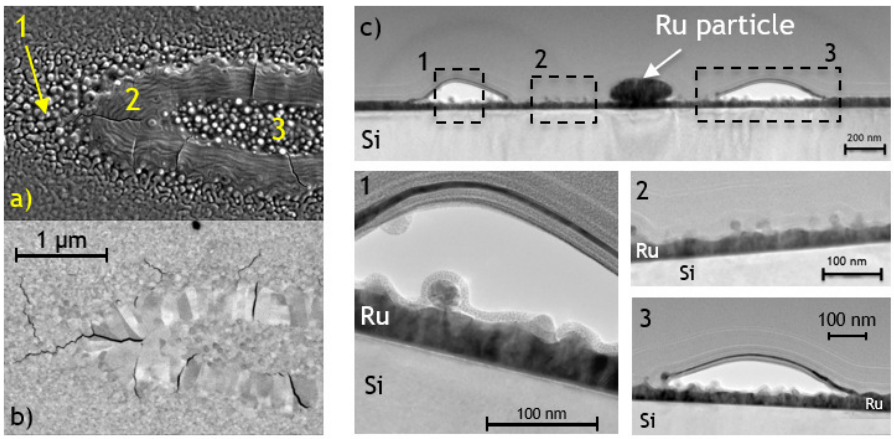

Fig. 2. (a) HR-SEM image of the damaged spot produced by the 100 fs XUV FEL pulse with an incident peak fluence $F = 234$ mJ/cm^2. (b) HR-SEM image of the same spot obtained with the ESB detector. (c) TEM cross-section made at the center along the short axis of the damaged spot produced by the 100 fs XUV FEL pulse with an incident peak fluence of $F = 232$ mJ/cm^2. The spot has a similar morphology as the one shown in (a) and (b).

Ex-situ analysis of the damage morphologies was performed by means of differential interference contrast microscopy (DIC) with a Nomarski prism, high-resolution scanning electron microscopy (HR-SEM), transmission electron microscopy (TEM) and atomic force microscopy (AFM).

2.1. *Ex-situ analysis of damaged spots*

We report a detailed analysis of the damage morphologies in the energy range of $\sim 0.2 - 0.6$ μJ per pulse, which corresponds to a peak fluence range of $\sim 190 - 500$ mJ/cm^2. By applying higher fluences we start to damage the Si substrate underneath Ru, studying which is beyond the focus of the present work.

HR-SEM image of the damaged spot produced by the laser pulse with an incident fluence of $F = 213$ mJ/cm^2 is shown in Fig. 1(a). This is the minimal damage detectable by means

Optics EXPRESS

of HR-SEM. Note that DIC microscopy is not able to resolve such minor surface changes. A damaged spot with a lateral size of about 4.5 μm is observed and can be characterized as increased surface roughness and cracks. The roughness gradually decreases from the center of the spot towards the edge, which is confirmed with the AFM line profile taken in the center along the short axis of the spot, Fig. 1(b). No other signatures of damage such as compaction of Ru layer were detected.

Different morphology is observed when irradiating the target with slightly higher fluences. The damaged spot produced with an incident fluence of $F = 234$ mJ/cm^2 is shown in Fig. 2(a). Three distinct regions can be distinguished: nanoroughness and cracks at the edge (region 1), similar to that observed in Fig. 1(a), a smooth "ring" structure with cracks (region 2) and spherical nanofeatures in the center of the spot (region 3). The lateral size of the nanofeatures varies in the range of $\sim 20 - 70$ nm. The HR-SEM image obtained with an energy selective backscattered (ESB) detector is shown in Fig. 2(b). This detector enables one to resolve the elemental composition of the surface of the material under investigation. Since the difference in atomic number between Si and Ru is large, these elements result in a very different contrast. The ESB image shows that the surface consists of Ru only, while the cracks reach down to the Si substrate. The grain structure of the damaged spot happened to be better resolved with the ESB detector, since this detector is also sensitive to the atomic planes orientation. Interestingly, the grains in region 2, having an increased size and asymmetrical shape, are different from the grains in region 1 and 3 and in the non-irradiated region.

TEM cross-section is made in one of the spots that have a similar morphology as the spot in Fig. 2(a,b). The cross-section is made in the center along the short axis of the spot. During sample preparation, a layer of Pt was deposited on top of Ru to protect the surface from focused ion beam cycles. The results are shown in Fig. 2(c), revealing the in-depth structure of the damaged spot. The TEM image shows that the smooth "ring" region observed with HR-SEM is a delaminated top layer of Ru. The thickness of that layer varies from 5 to 16 nm being the thickest in the part where it is still connected to the sample and decreasing towards the far end. At the center of the spot, where the local fluence is higher than at the edge, the delaminated layer is

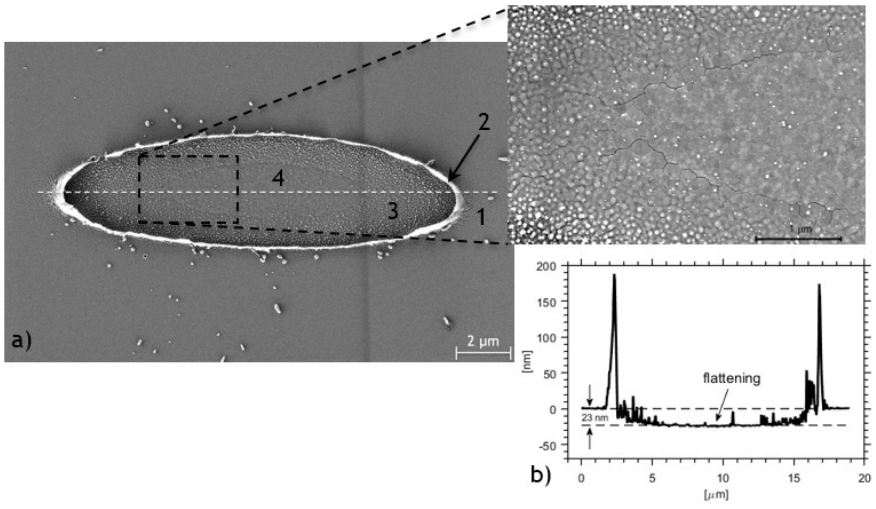

Fig. 3. (a) HR-SEM image of the damaged spot produced by the 100 fs XUV FEL pulse with an incident peak fluence of $F = 374$ mJ/cm^2. The dashed horizontal line indicates where the AFM line profile is made. (b) AFM line profile illustrating the flat bottom in the central part of the damage crater.

Optics EXPRESS

either completely removed (as in the spot shown in Fig. 2(a), region 3) or remained at the surface in the form of a large Ru particle, Fig. 2(c). Spherical nanofeatures in the center of the spot and below the delaminated layer seem to be droplets of molten and resolidified Ru. The remaining thickness of the Ru in the central part is measured to be roughly 35 nm, which corresponds to the thickness of the delaminated layer in this part to be ~ 15 nm.

Figure 3 illustrates a typical damage spot produced by laser pulses with an incident peak fluence in the range of 327 – 458 mJ/cm^2. Same morphologies (nanoroughness 1, delaminated layer 2 and spherical nanofeatures 3) as in the previous stages of damage, Fig. 2, are observed with a new feature in the center of the spot (region 4). This region has a well-defined border in the form of a crack, see Fig. 3(a) magnification, and appears to be more flat compared to region 3. A line cross-section extracted from the AFM scan of the spot illustrates the flattening in the center, see Fig. 3(b). It also shows that the depth of the crater does not extend into the Si substrate. The thickness of the delaminated layer in the center of the spot is estimated to be ~ 23 nm. Low density of nanofeatures in region 4 (white dots in the HR-SEM images) enables one to resolve the grain structure of the surface in this region. Separate grains are clearly observed and are larger than the grains in the non-irradiated part of Ru surface.

Delamination or *spallation* induced by ultra-short laser pulses in metal targets is a phenomenon that was extensively studied in literature, but in case of irradiation with optical lasers [18, 32]. The damage morphologies in Ru that we observe in our experiments with XUV light resemble the same features. In the discussion part, based on our calculations, we suggest that the mechanism responsible for the XUV single-shot ablation of Ru is the same as was previously reported for the case of damage with optical lasers, namely, photomechanical spallation.

2.2. Damage threshold determination

Two types of morphologies detected during *ex-situ* analysis of the damaged spots exhibit clear threshold behavior: spallation and flattening of the surface in the center of the spot. The damage threshold values for both processes are obtained using the Liu's plot method [33], where the dependence of the damaged area on the peak fluence is plotted on a semilogarithmic scale, Fig. 4. The spallated areas are measured using DIC microscopy. For the second type of morphology the HR-SEM images are used to measure the areas surrounded by the crack, region 4 in Fig. 3(a), since

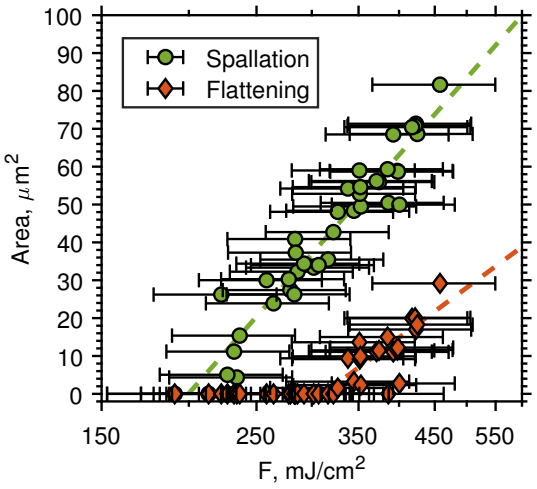

Fig. 4. Liu's plot for the two damage threshold processes: spallation (circles) and flattening in the center of the crater (diamonds). The dashed lines represent the best fit of the experimental data.

Optics EXPRESS

DIC microscopy was not accurate enough to resolve such fine features of the damage morphology. By extrapolating the linear fit of the experimental data to zero damaged area, we determine the spallation and flattening thresholds to be $F_{th}^{spal} = 200 \pm 40$ mJ/cm^2 and $F_{th}^{flat} = 311 \pm 62$ mJ/cm^2 respectively. Data points with zero damage area are not taken into account in the fitting procedure. The uncertainty of the presented approach is mostly determined by the error of peak fluence determination since the uncertainty of the damage area measurement is much lower ($\sim 1.5\%$).

3. Simulations

In this part we describe the XCASCADE(3D) [22] and the TTM [23] that are used to simulate the interaction of the XUV femtosecond laser pulse with a thin Ru film. Within the XCASCADE(3D) approach, the target is assumed to be a homogeneous arrangement of atoms (atomic approximation) with a density corresponding to the chosen material. The code uses an event-by-event Monte Carlo simulation scheme. For simulations of photoabsorption, the cross sections are taken from the EPDL97 database [34]. A photoelectron receives an amount of energy equal to the difference between the photon energy and the ionization potential of the corresponding atomic shell, extracted from the EADL database [35].

Electron propagation is simulated using atomic binary-encounter-Bethe (BEB) cross sections of the impact ionization [36] and Mott's atomic cross sections for the elastic collisions [37]. In an impact ionization event, an incident electron triggers emission of a secondary electron from an atomic shell chosen according to relative cross sections [38]. In an elastic scattering event, an incident electron scatters on an atom without energy loss, so only the direction of electron propagation changes. The scattering angle of an incident electron in both scattering processes is calculated using the anisotropic scattering scheme, described in [22]. The scattering angle of the impact-ionized electron follows from the momentum conservation law.

The XCASCADE(3D) code provides a good description of electron cascades in the regime of "low" fluence. The latter means that: (i) the electrons are non-interacting and the electron cascades develop independently, i.e. the density of high-energy electrons participating in the cascading is at least ten times less than the atomic density and (ii) the material properties are not affected during the electron cascading, i.e. the photoionization and impact ionization cross sections do not change significantly. Correspondingly, cross sections for the unexcited material are applied.

The holes created in atomic core-levels recombine via an Auger decay process releasing an Auger electron, which is the dominant recombination channel for outer atomic shells. When impact ionization or a core hole decay generate a valence hole, its energy and position are recorded. Within the atomic approximation we consider that the energy stored in the valence holes corresponds to the energy of thermalized electrons in the conduction band in a real metal system.

Polarization of light is known to affect the direction of photoelectrons. Separate XCASCADE(3D) calculations were performed to estimate the influence of polarization on the development of electron cascades. Two limiting cases were compared. In the first one, the direction of photoelectrons was chosen to be isotropic (no polarization assumed). In the second case, we chose the direction of photoelectrons to be perpendicular to the surface (up and down, mimicking p-polarization under grazing incidence). The results showed only insignificant difference proving that the role of the polarization is small for the conditions considered in this work.

All photo- as well as secondary electrons are traced until their energy falls below a cut-off energy, which is chosen to be 10 eV [22, 38]. As soon as an electron loses its energy below this cut-off, it is considered as a slow electron thermalized in the conduction band of the material. The Monte Carlo simulations are repeated $> 10^5$ times for sufficient statistics to provide reliable results.

To calculate the energy density depth profiles we first perform simulations for bulk material

Optics EXPRESS

assuming all photons are absorbed at $z = 0$ ("surface"). Here and further z denotes the in-depth direction. Then the realistic absorption positions are taken into account by applying a convolution with the Lambert-Beer's law taking the light penetration depth corresponding to the particular angle of incidence. Here we treat the region $z \geq 0$ as Ru, while region $z < 0$ is considered as vacuum above the Ru surface. This approach enables one to estimate the total energy emitted from the sample, but not the actual distribution of energy above the surface.

As a result, we obtain the energy density of the thermalized electrons, $U_e(\boldsymbol{r}, t)$, and valence holes, $U_h(\boldsymbol{r}, t)$, as functions of space and time. The time derivative of the total energy density $U = U_e + U_h$ is used to calculate the source term for the TTM.

The TTM is formulated as a set of two coupled nonlinear differential equations, which describe the spatial and temporal evolution of electron (T_e) and lattice (T_l) temperatures:

$$\begin{cases} C_e(T_e)\dfrac{\partial T_e}{\partial t} = \dfrac{\partial}{\partial z}\left(k_e(T_e, T_l)\dfrac{\partial T_e}{\partial z}\right) - G(T_e)(T_e - T_l) + S(z,t) \\ \\ C_l(T_l)\dfrac{\partial T_l}{\partial t} = G(T_e)(T_e - T_l), \end{cases} \tag{1}$$

where C_e and C_l are the electron and lattice heat capacities, respectively, k_e is the electron thermal conductivity, G is the electron-phonon coupling factor, which describes the energy exchange rate between electrons and the lattice, and $S(z, t)$ is the heat source. All thermal parameters are temperature-dependent (see Appendix for details). The problem is formulated in only one, in-depth, dimension, since the laser spot size ($\sim \mu$m) is much larger than the penetration depth of the radiation ($\sim$ nm), which makes the temperature gradients in lateral direction much smaller than in the in-depth direction.

As a source term, we use the time derivative of the total energy density $U(z, t)$ inside the Ru film, projected into the in-depth direction z:

$$S(z,t) = \frac{\partial U(z,t)}{\partial t}, \quad 0 \leq z \leq L, \tag{2}$$

where L is the film thickness. To evaluate the importance of the non-equilibrium electron kinetics stage, we also perform the TTM calculations without XCASCADE(3D) using a standard source term, representing heating of the electronic system with a temporally Gaussian laser pulse with exponential decay of the absorbed energy:

$$S(z,t) = \sqrt{\frac{4ln2}{\pi}}\frac{F(1-R)}{\delta\tau_p}e^{-z/\delta}e^{-4ln2\left(t/\tau_p\right)^2}, \tag{3}$$

where F is the incident fluence, R is the surface reflectivity, δ is the light penetration depth and τ_p is the pulse duration. With this standard TTM approach it is assumed that electrons are always in thermal equilibrium during the heating process.

We neglect the lattice thermal conductivity since electrons are considered as the main heat carriers in metals. The system (1) is solved numerically using the finite-difference method with Neumann boundary conditions (no heat flux at both interfaces). Both electrons and lattice are at room temperature $T_0 = 300\ K$ at the beginning of the simulations. The choice of thermal and optical parameters is described in Appendix.

Melting of the Ru film is simulated within the TTM taking the latent heat of melting H_m into account using the enthalpy method [39]. The lattice temperature is reconstructed from the relationship between enthalpy and lattice temperature, taken from [40]. Here for simplicity we neglect the difference in thermal properties between the liquid and solid phase.

In the following two sections we present the results of the XCASCADE(3D) and TTM calculations. The incident fluence level used in most of the calculations in this work is chosen to

Optics EXPRESS

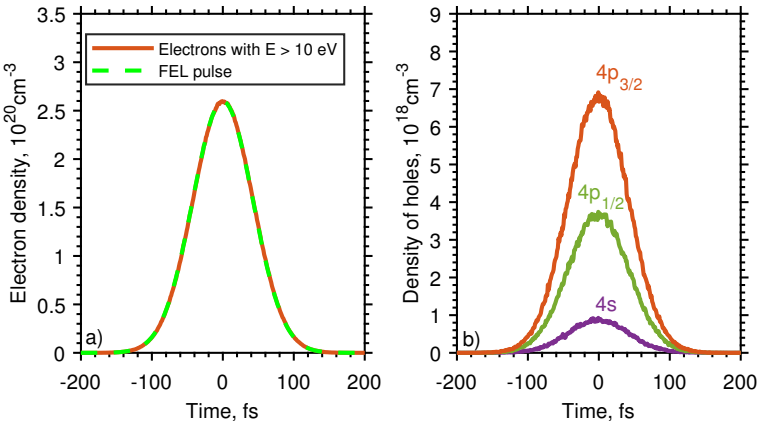

Fig. 5. (a) Transient integral density of excited electrons with energy above the cut off threshold of 10 eV (solid line). The Gaussian temporal profile of a 100 fs FEL pulse is shown schematically with a dashed line. (b) Transient integral density of holes created in $4s$, $4p_{1/2}$ and $4p_{3/2}$ levels of Ru. The incident fluence is $F = 200$ mJ/cm^2.

be $F = 200$ mJ/cm^2, which is the spallation threshold measured in the experiment.

3.1. Results of the XCASCADE(3D) calculations

Transient number and energy densities of electrons and deep-shell holes generated in Ru with 92 eV photons and 200 mJ/cm^2 incident fluence are calculated with the XCASCADE(3D) code. Figure 5 presents the integral densities of (a) cascading electrons and (b) deep-shell holes. We assume a Gaussian temporal profile of the laser pulse in the simulations of photoabsorption. Here and further, $t = 0$ corresponds to the moment of time when the maximum of the laser pulse intensity is at the surface of the Ru film. The density of electrons participating in the cascading, i.e. those with an energy above the cut off threshold of 10 eV, follows closely the Gaussian temporal profile of the FEL pulse with 100 fs FWHM, Fig. 5(a), which shows that there is virtually no cascading after the laser pulse. The duration of electron cascades in Ru at this photon energy, defined as FWHM of the electron density increase [38], is found to be < 1 fs. Please note, that the density of cascading electrons is much lower than the atomic density of Ru ($7.4 * 10^{22}$ cm^{-3}), ensuring the applicability of the XCASCADE(3D) code.

A photon with an energy of 92 eV is capable of ionizing 4s, 4p, 4d and 5s electrons in Ru. The 4d and 5s valence levels in our atomic approximation represent the conduction band of the material, and, thus, photoabsorption by these electrons is considered simply as heating of the conduction band electronic system. The holes, created in those levels do not recombine via Auger processes, and the energy stored in these holes is treated as the energy of electrons thermalized in the conduction band.

The 4s-, 4p$_{1/2}$- and 4p$_{3/2}$-level holes have characteristic Auger or Coster-Kronig decay times of 0.04 fs, 0.13 fs and 0.12 fs, respectively [35]. Thus, they are quickly decaying into the conduction band within the pulse duration, see Fig. 5(b).

For the heat source in the TTM, we need the spatiotemporal distributions of the energy density of thermalized electrons, $U_e(z,t)$, and valence holes, $U_h(z,t)$, which are obtained from the XCASCADE(3D) calculations. The time derivative of the total energy density $\partial U(z,t)/\partial t = \partial(U_e(z,t) + U_h(z,t))/\partial t$ is used to generate the heat source. The resulting 2D map of the power density $\partial U(z,t)/\partial t$ is shown in Fig. 6(a). The first 20 nm of the 50 nm thick Ru film are shown together with 5 nm of vacuum above the Ru surface. One can see that most of the energy (92%) stays inside the Ru, while 8% escapes from the surface via electron emission. The

Optics EXPRESS

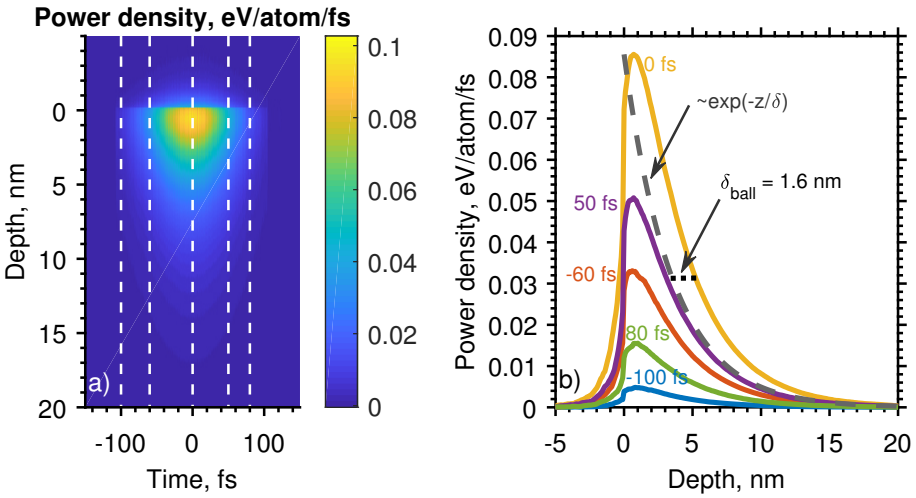

Fig. 6. (a) 2D map of temporal and spatial evolution of the power density $\partial U(z,t)/\partial t$ of thermalized electrons and valence holes obtained from XCASCADE(3D) calculations with an incident fluence of $F = 200$ mJ/cm^2. The top 20 nm of the total 50 nm thick Ru film are shown. The surface of the Ru film is at $z = 0$, and the region $z < 0$ corresponds to the vacuum above the surface. (b) Power density depth profiles at different times (solid lines). The times are indicated in (a) with vertical dashed lines. For comparison, the Lambert-Beer's exponent is shown schematically with a dashed line.

values are obtained by integrating the power density below and above the surface, respectively. The energy escapes via photo- and secondary electrons that have sufficient energy to travel to the surface and overcome the work function of Ru (4.7 eV).

Figure 6(b) illustrates the depth profiles of the power density $\partial U(z,t)/\partial t$ at different moments of time, indicated with vertical dashed lines in Fig. 6(a). The average distance electrons travel before thermalization (electron ballistic range) can be extracted. The spatial profiles in Fig. 6(b) are the result of convolution with the Lambert-Beer's exponent $exp(-z/\delta)$ with light penetration depth $\delta = 3.5$ nm (20° grazing incidence). Therefore, the actual electron ballistic range δ_{ball} is obtained as the difference between the final profile (solid lines) and the Lambert-Beer's exponent (dashed line) at $1/e$ level. Following this procedure, the electron ballistic range in Ru is found to be 1.6 nm in case of irradiation with 92 eV photons.

In summary, our XCASCADE(3D) calculations show a small electron cascading effect in Ru under XUV exposure. Excited electrons thermalize within < 1 fs and travel only 1.6 nm ballistically before thermalization. About 8% of the absorbed energy escapes from the surfaces due to high-energy electron emission. Note, however, that we expect longer cascading times and electron ranges with increase of the photon energy.

3.2. *Results of the two-temperature model calculations*

In this section we present the results of the TTM calculations of electron and lattice temperature evolution, Eq. (1). As a heat source for the TTM we use the time derivative of the total energy density $U(z,t)$ inside the Ru film, Eq. (2) with $L = 50$ nm. In that way, only the energy that stays inside the Ru film is taken into account in the TTM calculations. The results are compared with the TTM calculations with a standard heat source, Eq. (3).

Figure 7 shows the temporal evolution of electron and lattice temperatures at the front surface of the Ru film. Solid lines are the results of the TTM calculations with the XCASCADE(3D) heat source, Eq. (2). There is strong thermal non-equilibrium between electrons and lattice just

Optics EXPRESS

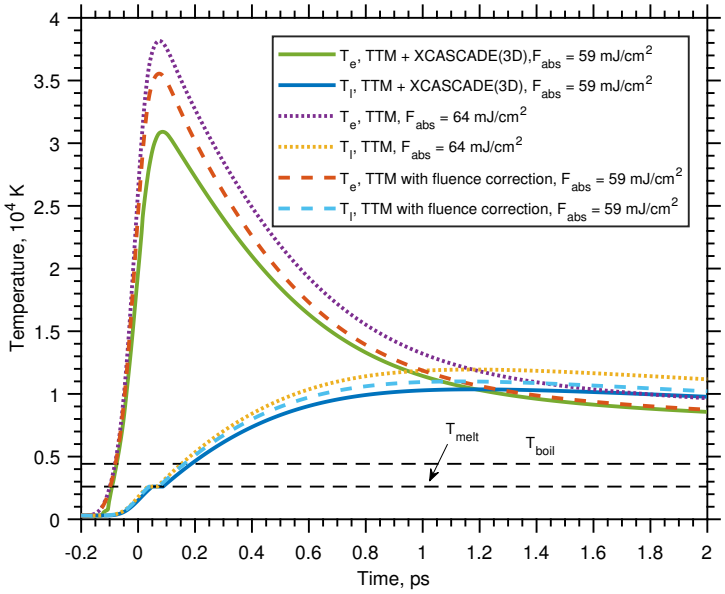

Fig. 7. Temporal evolution of electron (T_e) and lattice (T_l) surface temperatures of a 50 nm Ru film irradiated by a 100 fs XUV pulse with an incident fluence of $F = 200$ mJ/cm^2, calculated with different approaches. Solid lines are the results of the TTM calculations with the XCASCADE(3D) heat source. Dotted and dashed lines show the results of the TTM calculations with a standard heat source without and with the 8% fluence correction taking into account the electron emission, respectively. Black dashed horizontal lines indicate the melting (2607 K) and boiling (4423 K) temperatures of Ru under normal conditions.

after the absorption of the FEL pulse, with electrons having significantly higher temperature than the lattice. The non-equilibrium occurs since the pulse duration of 100 fs is shorter than the electron-phonon thermalization time τ_{el-ph} [24]. The latter is calculated from the TTM results as the time when the difference between electron and lattice temperatures at the surface decreases to the $1/e$ level and is equal to $\tau_{el-ph} \sim 0.5$ ps. The incident fluence level of $F = 200$ mJ/cm^2 corresponds to the absorbed fluence of $F_{abs} = F(1-R)(1-\alpha) = 59$ mJ/cm^2, where α is the fraction of energy emitted from the surface obtained from the XCASCADE(3D) calculations (8%).

The dotted lines are the results of the TTM calculations with a standard heat source, Eq. (3). The absorbed fluence in that case is $F_{abs} = F(1-R) = 64$ mJ/cm^2, since electron emission from the surface is not taken into account in the standard TTM approach. As expected, the temperatures are overestimated since the absorbed fluence is higher compared to the TTM + XCASCADE(3D) calculations.

In order to take into account the electron emission within the TTM, we decrease the absorbed fluence by 8% in the TTM calculations with a standard heat source (dashed lines). The results are closer to the ones obtained with the TTM + XCASCADE(3D) approach. The 13% difference at the electron temperature peak is due to the fact that in the TTM + XCASCADE(3D) calculations, before thermalization, electrons travel ballistically for a distance of 1.6 nm, see Fig. 6, which effectively increases the volume where the energy was absorbed. This results in a lower peak value of the electron temperature compared to the standard TTM calculations where ballistic transport is not taken into account. The difference becomes smaller with time (2% at $t = 2$ ps), since the diffusion of thermalized electrons dominates the ballistic transport of electrons after thermalization. The diffusion length L_c, which is the distance electrons travel diffusively before

Optics EXPRESS

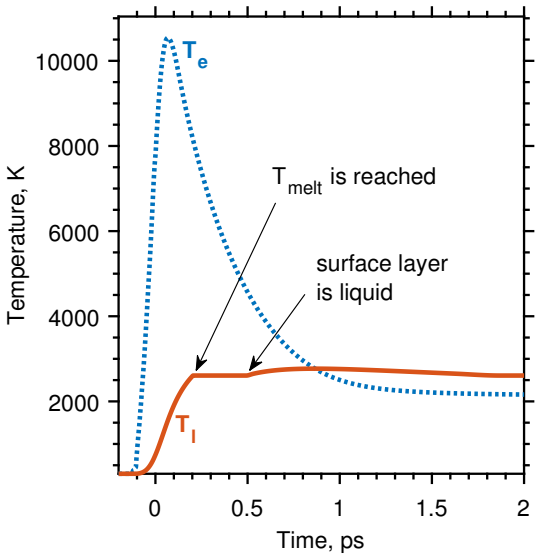

Fig. 8. Temporal evolution of electron (dotted line) and lattice (solid line) surface temperatures of a 50 nm Ru film irradiated by a 100 fs XUV pulse with an absorbed fluence of F_{abs} = 14 mJ/cm^2, calculated with the TTM + XCASCADE(3D) approach.

thermal equilibration with the lattice at the surface, can be extracted from the electron temperature profile at $t = \tau_{el-ph}$ as the depth where the temperature decreases to $1/e$ level. It is found to be $\sim$ 10 nm, which is $\sim$ 6 times larger than the ballistic range. The difference in the lattice temperatures at the surface between the TTM calculations with the fluence correction and those with the XCASCADE(3D) source term stays below 10%.

This comparison suggests that although using the XCASCADE(3D) source term we obtain lower electron temperatures just after the absorption of the laser pulse compared to the standard TTM calculations due to the effects of electron emission from the surface and electron ballistic transport, neither of these effects has a significant impact on the dynamics of the lattice heating, which is the crucial process in the damage mechanism, as will be shown in the discussion section.

The lattice temperature plateau at T_l = 2607 K, Fig. 7, corresponds to the melting process. The surface of Ru reaches the melting temperature at the beginning and becomes liquid at the end of the plateau. The melting threshold can thus be determined as the incident fluence required to melt the front surface of Ru. With a separate set of TTM + XCASCADE(3D) calculations we determine the melting threshold to be F_{th}^{melt} = 44 mJ/cm^2, corresponding to the absorbed fluence of F_{abs} = 13 mJ/cm^2, which is 5 times lower than the spallation threshold, observed in the experiment. That suggests that melting occurs before spallation, which is also supported by our experimental observations. Figure 8 illustrates the onset of melting showing the evolution of electron and lattice surface temperatures for an absorbed fluence of F_{abs} = 14 mJ/cm^2.

Further, we present the lattice temperature evolution on a longer timescale compared to Fig. 7, in order to illustrate the melting dynamics of the top part of the Ru film. The corresponding TTM + XCASCADE(3D) simulations are performed for a 100 nm thick film. The thickness is increased compared to the 50 nm Ru used in the experiment, so that the heat flux into the thick Si substrate is also modeled, albeit in a simplified way, where the bottom 50 nm of Ru in the calculations represent the substrate. In order to select the optimal thickness of the film we perform calculations with increasing thickness until convergence of the results is reached.

The 2D map of the lattice temperature as a function of depth and time calculated for the absorbed fluence of F_{abs} = 59 mJ/cm^2 is shown in Fig. 9. This fluence level corresponds to the

Optics EXPRESS

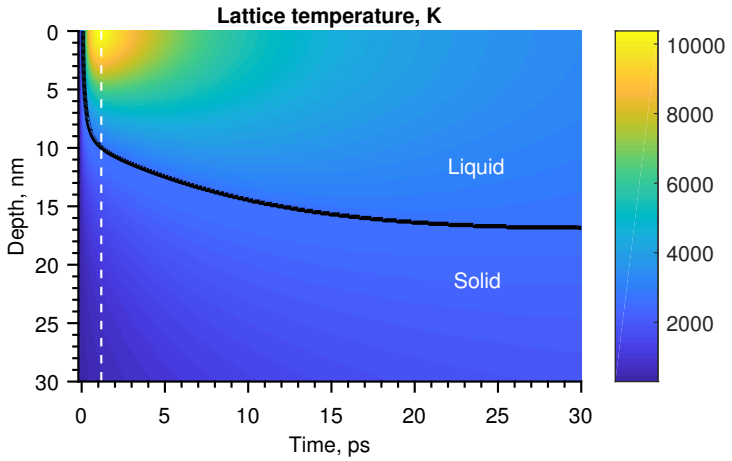

Fig. 9. 2D map of temporal and spatial evolution of the lattice temperature of a 100 nm thick Ru film calculated with the TTM + XCASCADE(3D) approach for an absorbed fluence of F_{abs} = 59 mJ/cm^2. Black solid line shows the interface between solid and liquid Ru. The top 30 nm of the total 100 nm thick Ru film are shown. The white dashed line plotted at the moment of time when $T_e = T_l$ at the surface separates the two melting regimes: fast melting of the top 10 nm of Ru and subsequent slow propagation of the solid-liquid interface for another 7 nm.

onset of spallation observed in the experiment. Thus, the lattice temperature behavior presented in Fig. 9 can be treated as melting of the top Ru layer that occurs just before spallation (in terms of fluence). The black solid line marks the border between the liquid and the solid phases of Ru. Fast melting of the top 10 nm during the first 1.2 ps is followed by a much slower propagation of the melting front into the depth of the material. Similar two-step melting dynamics was previously reported for other metals [17, 27]. The melting starts at 0.08 ps and the maximum melted depth of 17 nm is reached at 30 ps after the laser pulse. The vertical white dashed line, plotted at the moment of time when $T_e = T_l$ at the surface, see Fig. 7, separates the two melting regimes. Hence, the fast melting of the top 10 nm is due to the diffusion of hot electrons and transfer of their energy to the lattice during the thermal non-equilibrium stage, while the second melting stage is a slow propagation of the solid-liquid interface after electrons and lattice equilibration. The calculated maximum melted depth (17 nm) is larger than the estimated thickness of the spallated layer observed in the experiment at a comparable fluence ($\sim 5 - 16$ nm), see Fig. 2(c), which indicates that the spallation occurs inside the liquid layer.

4. Discussion

The experimentally observed features of XUV-induced ablation of the Ru film resemble the phenomenon of photomechanical spallation in metal targets induced by optical lasers. It was shown that the generation of a thermo-induced compressive stress wave followed by a tensile stress wave propagating in the irradiated target is the cause of spallation [17, 18, 32, 41, 42]. Large stresses are generated because the heating of the lattice is faster than the time needed for the system to mechanically react to that ultrafast heating by expanding. This situation is referred to as the *stress confinement regime*, which occurs under the following conditions: $\tau_{el-ph} \leq \tau_a$, where τ_{el-ph} is the electron-phonon thermalization time which represents the characteristic time of lattice heating and τ_a is the acoustic relaxation time. From our calculations we obtain that $\tau_{el-ph} = 0.5\ ps$, see Fig. 7. Acoustic relaxation time can be estimated as $\tau_a \sim L_c/C_s$, where $L_c \sim 10$ nm is the diffusion length described above, and C_s is the bulk speed of sound. The latter

Optics EXPRESS

is calculated as $C_s = \sqrt{B/\rho} \sim 5000$ m/s, where B is the bulk modulus and ρ is the density of Ru. Thus, $\tau_a \sim 2$ ps and the condition of the stress confinement regime is satisfied. Therefore, we conclude that the mechanism responsible for the XUV induced single-shot ablation of Ru is photomechanical spallation in the stress confinement regime.

As one can see from Fig. 7, the incident fluence level of 200 mJ/cm^2 is sufficient not only to melt the surface of Ru, but also to heat the resulting liquid up to ~ 2.5 times above the boiling temperature at atmospheric pressure ($T_{boil} = 4423$ K). Although such high temperatures are reached, boiling is not considered here as a damage mechanism since homogeneous explosive boiling with a vapor bubble nucleation rate of the order of $J \sim 10^{36}$ m^{-3}s^{-1} is only possible in close vicinity of the critical point of the material [43, 44]. The bubble nucleation rate is determined using the heated depth of about $L_c \sim 10$ nm and the acoustic time of $\tau_a \sim 2$ ps, which were determined above, as $J = 1/(L_c^3 \tau_a)$. The morphology of damage craters also does not support the idea of boiling to be the damage mechanism.

Our XCASCADE(3D) calculations support the hypothesis that XUV-induced spallation in Ru has the same nature as spallation in metals induced by optical lasers. Namely, the electron cascading effect is found to be small: electrons thermalize very quickly within the pulse duration and travel ballistically for a short distance before thermalization. Only a small part of the absorbed energy escapes from Ru via electron emission.

Electron thermal diffusion length is found to dominate both the light penetration depth and the electron ballistic range. Therefore, despite the difference in the light penetration depth between XUV used in our experiment and optical lasers, electrons should diffuse the absorbed energy over comparable volumes, which should result in the same damage process – photomechanical spallation. Hence, according to our investigations, XUV light does not introduce any other significant effects into the single-shot damage process compared to visible light.

Within the proposed damage mechanism, we suggest the explanation of some of the damage morphologies observed in our experiment, using the analogy with the optical damage studies. The absorption of the high fluence femtosecond laser pulse first results in the ultrafast melting of the top part of the Ru film. The depth of melting depends on the incident fluence and is equal to 17 nm for $F = 200$ mJ/cm^2 according to our calculations, Fig. 9. If the fluence of the pulse is below the spallation threshold of $F_{th}^{spal} = 200 \pm 40$ mJ/cm^2, the melted layer of Ru cools down and recrystallizes, which may result into increased surface roughness. The fact that we did not observe compaction of Ru layer can be supported by the argument that Ru is magnetron deposited on top of a wafer, so the sample already has near bulk density.

During this pre-spallation stage cavitation below the surface typically occurs as a result of propagation of a tensile stress wave in the melted material [18, 32, 41, 45]. When the absorbed energy is not sufficient to cause complete spallation, the cavities in the cavitation zone collapse due to the surface tension. If the recrystallization front from the depth of the metal arrives before the collapse, the cavities may remain frozen below the surface [46–48]. The existence of such frozen cavities may also explain the nanoroughness observed in the pre-spallation stage, Fig. 1 and region 1 in Figs. 2(a) and 3(a), although detailed atomistic calculations are required to confirm this hypothesis.

When the incident fluence overcomes the spallation threshold, spallation of the top $6 - 23$ nm of Ru occurs, see Figs. 2 and 3. Increased grain size in the spallated layer, that remained attached to the surface, see Fig. 2(b), compared to the grains outside the damage spot, shows that the spallated layer was melted and resolidified having a different grain structure in the final state. During the spallation process the cavitation zone that is formed in the liquid layer by the tensile stress is stretched until it finally breaks [45]. Part of the liquid material between the spallated layer and the rest of the film is drawn into the spallated layer and the other part is attracted back to the bottom of the damage crater by the surface tension. As a result, spherical nanoparticles of Ru are observed at the bottom of the crater, Figs. 2 and 3.

Optics EXPRESS

The flattening in the center of the spot at even higher fluences, Fig. 3, can be explained as the interplay between two processes: rupture of the cavitation zone and arrival of the recrystallization front that propagates from the depth to the surface of the material. In the central part of the spot, where the local fluence is higher, the recrystallization front arrives much later than the rupture of the cavitation zone and subsequent spallation of the top part of the film, "freezing" the remaining liquid layer that had sufficient time to equilibrate into a smooth surface. At the edge of the spot, where the fluence is lower, the rupture of the cavitation zone occurs later, while the recrystallization front arrives earlier. As a result, the rough surface, that is formed just after spallation, is frozen. The existence of a similar flat central region in the damage crater of Al irradiated by 800 nm light [47], again, illustrates the similarities between XUV and optical damage of metals.

The fact that the calculated melting threshold of Ru is 5 times lower than the spallation threshold supports the assumption that melting takes place before spallation. A similar trend was reported for other metals damaged by optical lasers. It was calculated [17] that the melting threshold of bulk Ni irradiated with a 1 ps laser pulse is $\sim$ 5 times lower than the spallation threshold. Spallation starts inside the liquid layer of melted Ni with the thickness of the spallated layer smaller than the melted depth. The experimentally measured melting threshold of epitaxial Ag(001) [27] is $\sim$ 6 times lower than the fluence at which surface swelling of single-crystal Ag(001) was observed [48], which can be considered as the onset of spallation.

In our experiments we detect the surface modifications (roughening and cracks, Fig. 1) that happen before spallation in the incident fluence range from 190 to 213 mJ/cm^2. No exposures were performed with lower fluences. The minimum damage induced by 190 mJ/cm^2 pulses could only be detected by AFM measurements. Hence, we suggest that AFM is the most accurate microscopy technique to detect minor surface modifications produced by laser pulses.

In future work, we plan to supplement our model with detailed molecular dynamics simulations of melting, cavitation, spallation and possibly recrystallization processes. This would allow tracing the entire material evolution and benchmarking our model with the experimental data.

5. Summary and conclusions

We performed single-shot damage experiments at the free-electron laser FLASH, where 50 nm Ru films were exposed to 100 fs XUV (13.5 nm) pulses with varying fluences. The *ex-situ* analysis of the damaged spots revealed the following picture of damage development with increasing fluence. The first observable damage at the lowest applied fluence is roughening of the top surface of the Ru film. Melting and resolidification together with the possible existence of subsurface voids produced by a tensile stress wave propagating in the melted material are suggested as the processes responsible for increased surface roughness. The melting threshold is calculated as the incident fluence required to melt the top surface of Ru and is equal to $F_{th}^{melt} = 44$ mJ/cm^2. Spallation of the top $5 - 23$ nm of Ru was observed for fluences above the spallation threshold, which was measured to be $F_{th}^{spal} = 200 \pm 40$ mJ/cm^2. There are two types of morphologies observed inside the damage craters: spherical nanofeatures and flattening in the central part of the crater. The flattening occurs when the incident fluence is above the flattening threshold $F_{th}^{flat} = 311 \pm 62$ mJ/cm^2. The interplay between the rupture of the cavitation zone that is formed during the spallation process and the dynamics of resolidification may explain the observed morphologies inside the damage crater.

For better understanding of the observed damage morphologies we performed simulations of the interaction of the 100 fs XUV FEL pulse with a Ru target using the combined TTM + XCASCADE(3D) approach. We modeled the absorption of the laser pulse and the non-equilibrium electron kinetics with the Monte Carlo code XCASCADE(3D), while the diffusion of thermalized electrons and heating of the lattice were calculated with the two-temperature model. The results of the XCASCADE(3D) calculations were used as the heat source for the TTM. Based

Optics EXPRESS

on our calculations we suggest that the spallation observed in Ru under XUV exposure occurs in the stress confinement regime, similar to what was previously reported in studies of damage of metals with optical lasers. The results of XCASCADE(3D) calculations support the similarities between XUV- and optically-induced spallation, showing only a small electron cascading effect in Ru induced by XUV (92 eV) photons. Excited electrons thermalize within < 1 fs and travel ballistically over a distance of 1.6 nm before thermalization takes place. We calculated that $\sim 8\%$ of the absorbed energy escapes from the surface due to electron emission. Together with ballistic transport it affects the electron temperature just after the absorption of the FEL pulse, although both effects were found to have a small impact on the lattice temperature evolution, with the latter being crucial in understanding the single-shot damage mechanism. The presented computational analysis of non-equilibrium electron kinetics and ultrafast lattice heating can be applied to describe material response in a wide range of photon energies, provided that other conditions of applicability are met, which makes it a promising tool to study performance of materials under XUV and X-ray irradiation.

A. Thermal parameters

The accuracy of TTM depends on the proper choice of the thermal parameters of the material under investigation, especially in the regime of high electron temperatures, where these properties can significantly differ from their room temperature values. In our TTM calculations we reach the maximum values of electron temperature of the order of $3.5 * 10^4$ K, which is only ~ 3 times lower than the Fermi temperature $T_F = \epsilon_F / k_B \sim 9.9 * 10^4$ K of Ru [49], where k_B and ϵ_F are the Boltzmann constant and the Fermi energy, respectively. Therefore, the parameters that we use in the TTM calculations should be valid in the regime of high electron temperatures.

The dependencies of the electron heat capacity and electron-phonon coupling factor on the electron temperature are calculated using the formalism described in [50] within the effective one-band approximation and are shown in Fig. 10. The Ru density of states (DOS) is taken from [49]. The electron-phonon coupling factor is calculated within the harmonic approximation [50].

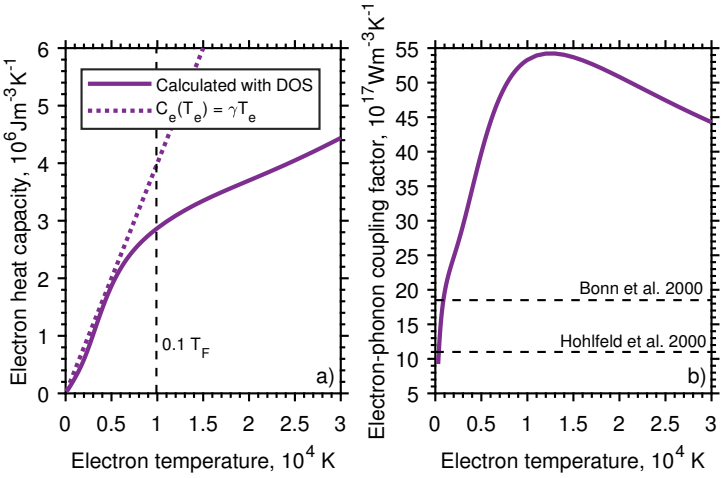

Fig. 10. Electron temperature dependence of the electron heat capacity (a) and electron-phonon coupling factor (b) calculated with the DOS of Ru taken into account (solid lines). Linear approximation for the electron heat capacity is shown with the dotted line in (a). The vertical dashed line at $T_e = 0.1 T_F$ approximately marks the limit of validity of the linear approximation for the electron heat capacity. The constant values of the electron-phonon coupling factor available in the literature are shown with dashed lines in (b).

Optics EXPRESS

The calculated electron heat capacity is compared with the linear approximation $C_e(T_e) = \gamma T_e$, with the electron specific heat constant γ taken from [51], see Fig. 10(a). A significant difference is observed in the high electron temperature region where the linear approximation is no longer valid. The latter is limited to the electron temperature range $0 < T_e < 0.1T_F$ [52,53].

Electron-phonon coupling G is strong in Ru, which is typical for transition metals. The calculated dependence of G on the electron temperature is shown in Fig. 10(b). The strong enhancement is followed by a decrease with a maximum value reached at $T_e \sim 1.2 * 10^4$ K. A similar behavior of G with increasing electron temperature was previously reported for titanium [54]. Both metals have hcp crystal structure and relatively low DOS at the Fermi level, which can explain the similar behavior. Our calculations are in a good agreement with previously reported values of G at room temperature [25,26].

The electron thermal conductivity is expressed as

$$k_e(T_e, T_l) = K \cdot \frac{(\vartheta^2 + 0.16)^{5/4}(\vartheta^2 + 0.44)\vartheta}{(\vartheta^2 + 0.092)^{1/2}(\vartheta^2 + b\,\vartheta_l)}, \tag{4}$$

where $\vartheta = k_B T_e/\epsilon_F$ and $\vartheta_l = k_B T_l/\epsilon_F$ [16,55]. K and b are material dependent constants. This expression is valid in a wide range of electron temperatures up to the temperatures considerably larger than the Fermi temperature. In order to determine K and b for Ru we fit Eq. (4) to the experimental curve of equilibrium thermal conductivity from [56] with K and b as fitting parameters, taking $T_e = T_l = T$ in Eq. (4). Values of thermal conductivity measured between 300 and 2500 K are used in the fitting procedure. Following this scheme we find $K = 35$ W/m/K and $b = 0.04$. Here we neglect phonon thermal conductivity in the metal and consider electron thermal conductivity to be equal to the total thermal conductivity.

The dependence of the lattice heat capacity on lattice temperature and the relationship between enthalpy and lattice temperature are taken from [40]. Surface reflectivity and light penetration depth are calculated using IMD software [57]. The summary of thermal and optical parameters used in this work is shown in Table 1.

Table 1. Parameter values used in calculations.

Electron specific heat constant[a]	$\gamma = 400$ J/m^3/K^2
Latent heat of melting[b]	$H_m = 4.7 * 10^9$ J/m^3
Surface reflectivity[c]	$R = 68\%$
Light penetration depth[c]	$\delta = 3.5$ nm
Pulse duration	$\tau_p = 100$ fs
Bulk modulus[d]	$B = 310$ GPa
Density[b]	$\rho = 12.3$ g/cm^3

[a]Ref. [51].
[b]Ref. [40].
[c]Ref. [57], at 13.5 nm wavelength, 20° grazing incidence.
[d]Ref. [58].

Funding

The Dutch Topconsortia Kennis en Innovatie (TKI) program on high-tech systems and materials (grant No. 14 HTSM 05); the Polish National Science Center (grant No. DEC-2011/03/B/ST3/02453; grant No. DEC-2012/06/M/ST3/00475); the EU FP7 EAGLE project

Optics EXPRESS

co-financed by the Polish Ministry of Science and Higher Education (grant No. REGPOT-CT-2013-316014); the Czech Science Foundation (17-05167S); the Czech Ministry of Education, Youth and Sports (grants CZ.02.1.01/0.0/0.0/16_013/0001552 [EF16_013/0001552] and LTT17015 [INTER-EXCELLENCE]); the Scientific Grant Agency of the Ministry of Education, Science, Research and Sport of the Slovak Republic and the Slovak Academy of Sciences (VEGA project No. 2/0021/16); the Slovak Research and Development Agency under the contracts No. APVV-15-0202 and APVV-14-0085.

Acknowledgements

We gratefully acknowledge the support of the operators of the FLASH facility, the Industrial Focus Group XUV Optics of the MESA+ Institute for Nanotechnology of the University of Twente, the industrial partners ASML and Carl Zeiss SMT GmbH, as well as the Province of Overijssel and The Netherlands Organisation for Scientific Research (NWO). We thank Mark Smithers, Enrico Keim and Henk van Wolferen for their help in performing the HR-SEM and TEM analysis, as well as Chris J. Lee, Frank Scholze, Vasily Zhakhovsky, Nail Inogamov, Viacheslav Medvedev, Cristina Sfiligoj, Joost Frenken, and Beata Ziaja for fruitful discussions.

References

1. W. Ackermann, G. Asova, V. Ayvazyan, A. Azima, N. Baboi, J. Bähr, V. Balandin, B. Beutner, A. Brandt, A. Bolzmann, R. Brinkmann, O. I. Brovko, M. Castellano, P. Castro, L. Catani, E. Chiadroni, S. Choroba, A. Cianchi, J. T. Costello, D. Cubaynes, J. Dardis, W. Decking, H. Delsim-Hashemi, A. Delserieys, G. Di Pirro, M. Dohlus, S. Düsterer, A. Eckhardt, H. T. Edwards, B. Faatz, J. Feldhaus, K. Flöttmann, J. Frisch, L. Fröhlich, T. Garvey, U. Gensch, C. Gerth, M. Görler, N. Golubeva, H.-J. Grabosch, M. Grecki, O. Grimm, K. Hacker, U. Hahn, J. H. Han, K. Honkavaara, T. Hott, M. Hüning, Y. Ivanisenko, E. Jaeschke, W. Jalmuzna, T. Jezynski, R. Kammering, V. Katalev, K. Kavanagh, E. T. Kennedy, S. Khodyachykh, K. Klose, V. Kocharyan, M. Körfer, M. Kollewe, W. Koprek, S. Korepanov, D. Kostin, M. Krassilnikov, G. Kube, M. Kuhlmann, C. L. S. Lewis, L. Lilje, T. Limberg, D. Lipka, F. Löhl, H. Luna, M. Luong, M. Martins, M. Meyer, P. Michelato, V. Miltchev, W. D. Möller, L. Monaco, W. F. O. Müller, O. Napieralski, O. Napoly, P. Nicolosi, D. Nölle, T. Nuñez, A. Oppelt, C. Pagani, R. Paparella, N. Pchalek, J. Pedregosa-Gutierrez, B. Petersen, B. Petrosyan, G. Petrosyan, L. Petrosyan, J. Pflüger, E. Plönjes, L. Poletto, K. Pozniak, E. Prat, D. Proch, P. Pucyk, P. Radcliffe, H. Redlin, K. Rehlich, M. Richter, M. Roehrs, J. Roensch, R. Romaniuk, M. Ross, J. Rossbach, V. Rybnikov, M. Sachwitz, E. L. Saldin, W. Sandner, H. Schlarb, B. Schmidt, M. Schmitz, P. Schmüser, J. R. Schneider, E. A. Schneidmiller, S. Schnepp, S. Schreiber, M. Seidel, D. Sertore, A. V. Shabunov, C. Simon, S. Simrock, E. Sombrowski, A. A. Sorokin, P. Spanknebel, R. Spesyvtsev, L. Staykov, B. Steffen, F. Stephan, F. Stulle, H. Thom, K. Tiedtke, M. Tischer, S. Toleikis, R. Treusch, D. Trines, I. Tsakov, E. Vogel, T. Weiland, H. Weise, M. Wellhöfer, M. Wendt, I. Will, A. Winter, K. Wittenburg, W. Wurth, P. Yeates, M. V. Yurkov, I. Zagorodnov, and K. Zapfe, "Operation of a free-electron laser from the extreme ultraviolet to the water window," Nat. Photonics **1**, 336–342 (2007).
2. E. Allaria, R. Appio, L. Badano, W. Barletta, S. Bassanese, S. Biedron, A. Borga, E. Busetto, D. Castronovo, P. Cinquegrana, S. Cleva, D. Cocco, M. Cornacchia, P. Craievich, I. Cudin, G. D'Auria, M. Dal Forno, M. Danailov, R. De Monte, G. De Ninno, P. Delgiusto, A. Demidovich, S. Di Mitri, B. Diviacco, A. Fabris, R. Fabris, W. Fawley, M. Ferianis, E. Ferrari, S. Ferry, L. Froehlich, P. Furlan, G. Gaio, F. Gelmetti, L. Giannessi, M. Giannini, R. Gobessi, R. Ivanov, E. Karantzoulis, M. Lonza, A. Lutman, B. Mahieu, M. Milloch, S. Milton, M. Musardo, I. Nikolov, S. Noe, F. Parmigiani, G. Penco, M. Petronio, L. Pivetta, M. Predonzani, F. Rossi, L. Rumiz, A. Salom, C. Scafuri, C. Serpico, P. Sigalotti, S. Spampinati, C. Spezzani, M. Svandrlik, C. Svetina, S. Tazzari, M. Trovo, R. Umer, A. Vascotto, M. Veronese, R. Visintini, M. Zaccaria, D. Zangrando, and M. Zangrando, "Highly coherent and stable pulses from the FERMI seeded free-electron laser in the extreme ultraviolet," Nat. Photonics **6**, 699–704 (2012).
3. F. Barkusky, A. Bayer, S. Doring, P. Grossmann, and K. Mann, "Damage threshold measurements on EUV optics using focused radiation from a table-top laser produced plasma source," Opt. Express **18**, 4346 (2010).
4. A. R. Khorsand, R. Sobierajski, E. Louis, S. Bruijn, E. D. van Hattum, R. W. E. van de Kruijs, M. Jurek, D. Klinger, J. B. Pelka, L. Juha, T. Burian, J. Chalupsky, J. Cihelka, V. Hajkova, L. Vysin, U. Jastrow, N. Stojanovic, S. Toleikis, H. Wabnitz, K. Tiedtke, K. Sokolowski-Tinten, U. Shymanovich, J. Krzywinski, S. Hau-Riege, R. London, A. Gleeson, E. M. Gullikson, and F. Bijkerk, "Single shot damage mechanism of Mo/Si multilayer optics under intense pulsed XUV-exposure," Opt. Express **18**, 700 (2010).
5. M. Muller, F. Barkusky, T. Feigl, and K. Mann, "EUV damage threshold measurements of Mo/Si multilayer mirrors," Appl. Phys. A **108**, 263–267 (2012).
6. A. Jody Corso, P. Zuppella, F. Barkusky, K. Mann, M. Müller, P. Nicolosi, M. Nardello, and M. Guglielmina Pelizzo, "Damage of multilayer optics with varying capping layers induced by focused extreme ultraviolet beam," J. Appl. Phys. **113**, 203106 (2013).

Optics EXPRESS

7. R. Sobierajski, S. Bruijn, A. Khorsand, E. Louis, R. E. van de Kruijs, T. Burian, J. Chalupsky, J. Cihelka, A. Gleeson, J. Grzonka, E. Gullikson, V. Hajkova, S. Hau-Riege, L. Juha, M. Jurek, D. Klinger, J. Krzywinski, R. London, J. B. Pelka, T. Płociński, M. Rasiński, K. Tiedtke, S. Toleikis, L. Vysin, H. Wabnitz, and F. Bijkerk, "Damage mechanisms of MoN/SiN multilayer optics for next-generation pulsed XUV light sources," Opt. Express **19**, 193 (2011).
8. S. P. Hau-Riege, R. A. London, R. M. Bionta, M. A. McKernan, S. L. Baker, J. Krzywinski, R. Sobierajski, R. Nietubyc, J. B. Pelka, M. Jurek, L. Juha, J. Chalupský, J. Cihelka, V. Hájková, A. Velyhan, J. Krása, J. Kuba, K. Tiedtke, S. Toleikis, T. Tschentscher, H. Wabnitz, M. Bergh, C. Caleman, K. Sokolowski-Tinten, N. Stojanovic, and U. Zastrau, "Damage threshold of inorganic solids under free-electron-laser irradiation at 32.5nm wavelength," Appl. Phys. Lett. **90**, 173128 (2007).
9. S. P. Hau-Riege, R. A. London, R. M. Bionta, D. Ryutov, R. Soufli, S. Bajt, M. A. McKernan, S. L. Baker, J. Krzywinski, R. Sobierajski, R. Nietubyc, D. Klinger, J. B. Pelka, M. Jurek, L. Juha, J. Chalupský, J. Cihelka, V. Hájková, A. Velyhan, J. Krása, K. Tiedtke, S. Toleikis, H. Wabnitz, M. Bergh, C. Caleman, and N. Timneanu, "Wavelength dependence of the damage threshold of inorganic materials under extreme-ultraviolet free-electron-laser irradiation," Appl. Phys. Lett. **95**, 111104 (2009).
10. S. P. Hau-Riege, R. A. London, A. Graf, S. L. Baker, R. Soufli, R. Sobierajski, T. Burian, J. Chalupsky, L. Juha, J. Gaudin, J. Krzywinski, S. Moeller, M. Messerschmidt, J. Bozek, and C. Bostedt, "Interaction of short x-ray pulses with low-Z x-ray optics materials at the LCLS free-electron laser," Opt. Express **18**, 23933 (2010).
11. J. Chalupský, V. Hájková, V. Altapova, T. Burian, A. J. Gleeson, L. Juha, M. Jurek, H. Sinn, M. Störmer, R. Sobierajski, K. Tiedtke, S. Toleikis, T. Tschentscher, L. Vyšín, H. Wabnitz, and J. Gaudin, "Damage of amorphous carbon induced by soft x-ray femtosecond pulses above and below the critical angle," Appl. Phys. Lett. **95**, 1–4 (2009).
12. S. Dastjani Farahani, J. Chalupsky, T. Burian, H. Chapman, A. Gleeson, V. Hajkoya, L. Juha, M. Jurek, D. Klinger, H. Sinn, R. Sobierajski, M. Störmer, K. Tiedtke, S. Toleikis, T. Tschentscher, H. Wabnitz, and J. Gaudin, "Damage threshold of amorphous carbon mirror for 177eV FEL radiation," Nucl. Instruments Methods Phys. Res. Sect. A **635**, S39–S42 (2011).
13. J. Pelka, R. Sobierajski, D. Klinger, W. Paszkowicz, J. Krzywinski, M. Jurek, D. Zymierska, A. Wawro, A. Petroutchik, L. Juha, V. Hajkova, J. Cihelka, J. Chalupsky, T. Burian, L. Vysin, S. Toleikis, K. Sokolowski-Tinten, N. Stojanovic, U. Zastrau, R. London, S. Hau-Riege, C. Riekel, R. Davies, M. Burghammer, E. Dynowska, W. Szuszkiewicz, W. Caliebe, and R. Nietubyc, "Damage in solids irradiated by a single shot of XUV free-electron laser: irreversible changes investigated using X-ray microdiffraction, atomic force microscopy and Nomarski optical microscopy," Radiat. Phys. Chem. **78**, S46–S52 (2009).
14. S. Nolte, C. Momma, H. Jacobs, A. Tünnermann, B. N. Chichkov, B. Wellegehausen, and H. Welling, "Ablation of metals by ultrashort laser pulses," J. Opt. Soc. Am. B **14**, 2716–2722 (1997).
15. J. Yang, Y. Zhao, N. Zhang, Y. Liang, and M. Wang, "Ablation of metallic targets by high-intensity ultrashort laser pulses," Phys. Rev. B **76**, 165430 (2007).
16. B. Rethfeld, D. S. Ivanov, M. E. Garcia, and S. I. Anisimov, "Modelling ultrafast laser ablation," J. Phys. D: Appl. Phys. **50**, 193001 (2017).
17. L. V. Zhigilei, Z. Lin, and D. S. Ivanov, "Atomistic modeling of short pulse laser ablation of metals: connections between melting, spallation, and phase explosion," J. Phys. Chem. C **113**, 11892–11906 (2009).
18. B. J. Demaske, V. V. Zhakhovsky, N. A. Inogamov, and I. I. Oleynik, "Ablation and spallation of gold films irradiated by ultrashort laser pulses," Phys. Rev. B **82**, 064113 (2010).
19. I. A. Makhotkin, R. Sobierajski, J. Chalupský, K. Tiedtke, G. de Vries, M. Störmer, F. Scholze, F. Siewert, R. W. E. van de Kruijs, I. Milov, E. Louis, I. Jacyna, M. Jurek, D. Klinger, L. Nittler, Y. Syryanyy, L. Juha, V. Hájková, V. Vozda, T. Burian, K. Saksl, B. Faatz, B. Keitel, E. Plönjes, S. Schreiber, S. Toleikis, R. Loch, M. Hermann, S. Strobel, H.-K. Nienhuys, G. Gwalt, T. Mey, and H. Enkisch, "Experimental study of EUV mirror radiation damage resistance under long-term free-electron laser exposures below the single-shot damage threshold," J. Synchrotron Radiat. **25**, 77–84 (2018).
20. T. Tsarfati, E. Zoethout, R. van de Kruijs, and F. Bijkerk, "Growth and sacrificial oxidation of transition metal nanolayers," Surf. Sci. **603**, 1041–1045 (2009).
21. A. Aquila, R. Sobierajski, C. Ozkan, V. Hájková, T. Burian, J. Chalupský, L. Juha, M. Störmer, S. Bajt, M. T. Klepka, P. Dłużewski, K. Morawiec, H. Ohashi, T. Koyama, K. Tono, Y. Inubushi, M. Yabashi, H. Sinn, T. Tschentscher, a. P. Mancuso, and J. Gaudin, "Fluence thresholds for grazing incidence hard x-ray mirrors," Appl. Phys. Lett. **106**, 241905 (2015).
22. V. Lipp, N. Medvedev, and B. Ziaja, "Classical monte-carlo simulations of x-ray induced electron cascades in various materials," Proc. SPIE **10236**, 102360H (2017).
23. S. Anisimov, B. Kapeliovich, and T. Perelman, "Electron emission from metal surfaces exposed to ultrashort laser pulses," Zh. Eksp. Teor. Fiz **66**, 776 (1974).
24. T. Qiu and C. Tien, "Heat transfer mechanisms during short-pulse laser heating of metals," J. Heat Transf. **115**, 835–841 (1993).
25. J. Hohlfeld, S.-S. Wellershoff, J. Güdde, U. Conrad, V. Jähnke, and E. Matthias, "Electron and lattice dynamics following optical excitation of metals," Chem. Phys. **251**, 237–258 (2000).
26. M. Bonn, D. N. Denzler, S. Funk, M. Wolf, S.-S. Wellershoff, and J. Hohlfeld, "Ultrafast electron dynamics at metal surfaces: competition between electron-phonon coupling and hot-electron transport," Phys. Rev. B **61**, 1101 (2000).
27. W.-L. Chan, R. S. Averback, D. G. Cahill, and A. Lagoutchev, "Dynamics of femtosecond laser-induced melting of

Optics EXPRESS

silver," Phys. Rev. B **78**, 214107 (2008).
28. K. Tiedtke, J. Feldhaus, U. Hahn, U. Jastrow, T. Nunez, T. Tschentscher, S. V. Bobashev, A. A. Sorokin, J. B. Hastings, S. Möller, L. Cibik, A. Gottwald, A. Hoehl, U. Kroth, M. Krumrey, H. Schöppe, G. Ulm, and M. Richter, "Gas detectors for x-ray lasers," J. Appl. Phys. **103**, 094511 (2008).
29. R. Sobierajski, M. Jurek, J. Chalupsky, J. Krzywinski, T. Burian, S. D. Farahani, V. Hajkova, M. Harmand, L. Juha, D. Klinger, R. a. Loch, C. Ozkan, J. B. Pelka, K. Sokolowski-Tinten, H. Sinn, S. Toleikis, K. Tiedtke, T. Tschentscher, H. Wabnitz, and J. Gaudin, "Experimental set-up and procedures for the investigation of XUV free electron laser interactions with solids," J. Instrumentation **8**, P02010 (2013).
30. J. Chalupsky, J. Krzywinski, L. Juha, V. Hajkova, J. Cihelka, T. Burian, L. Vysin, J. Gaudin, A. Gleeson, M. Jurek, a. R. Khorsand, D. Klinger, H. Wabnitz, R. Sobierajski, M. Stormer, K. Tiedtke, and S. Toleikis, "Spot size characterization of focused non-Gaussian X-ray laser beams," Opt. Express **18**, 27836 (2010).
31. J. Chalupský, T. Burian, V. Hájková, L. Juha, T. Polcar, J. Gaudin, M. Nagasono, R. Sobierajski, M. Yabashi, and J. Krzywinski, "Fluence scan: an unexplored property of a laser beam," Opt. Express **21**, 26363 (2013).
32. C. Wu and L. V. Zhigilei, "Microscopic mechanisms of laser spallation and ablation of metal targets from large-scale molecular dynamics simulations," Appl. Phys. A **114**, 11–32 (2014).
33. J. Liu, "Simple technique for measurements of pulsed gaussian-beam spot sizes," Opt. letters **7**, 196–198 (1982).
34. D. E. Cullen, J. H. Hubbell, and L. Kissel, "Epdl97: the evaluated photo data library97 version," Tech. rep., Lawrence Livermore National Lab., CA (United States) (1997).
35. S. Perkins, D. Cullen, M. Chen, J. Rathkopf, J. Scofield, and J. Hubbell, "Tables and graphs of atomic subshell and relaxation data derived from the llnl evaluated atomic data library (eadl), z= 1–100," Tech. rep., Lawrence Livermore National Lab., CA (United States) (1991).
36. Y.-K. Kim and M. E. Rudd, "Binary-encounter-dipole model for electron-impact ionization," Phys. Rev. A **50**, 3954 (1994).
37. I. Plante and F. A. Cucinotta, "Cross sections for the interactions of 1 eV-100 MeV electrons in liquid water and application to Monte-Carlo simulation of HZE radiation tracks," New J. Phys. **11**, 063047 (2009).
38. N. Medvedev, "Femtosecond X-ray induced electron kinetics in dielectrics: application for FEL-pulse-duration monitor," Appl. Phys. B: Lasers Opt. **118**, 417–429 (2015).
39. H. Hu and S. A. Argyropoulos, "Mathematical modelling of solidification and melting: a review," Model. Simul. Mater. Sci. Eng. **4**, 371 (1996).
40. A. E. Morris, H. A. Fine, and G. Geiger, *Handbook on Material and Energy Balance Calculations in Material Processing, Includes CD-ROM* (John Wiley Sons, 2011).
41. E. Leveugle, D. Ivanov, and L. Zhigilei, "Photomechanical spallation of molecular and metal targets: molecular dynamics study," Appl. Phys. A **79**, 1643–1655 (2004).
42. N. Nedialkov, S. Imamova, P. Atanasov, P. Berger, and F. Dausinger, "Mechanism of ultrashort laser ablation of metals: molecular dynamics simulation," Appl. Surf. Sci. **247**, 243–248 (2005).
43. V. P. Skripov, *Metastable liquids* (Wiley, 1974).
44. C. F. Delale, J. Hruby, and F. Marsik, "Homogeneous bubble nucleation in liquids: the classical theory revisited," The J. Chem. Phys. **118**, 792–806 (2003).
45. V. V. Zhakhovskii, N. A. Inogamov, and K. Nishihara, "New mechanism of the formation of the nanorelief on a surface irradiated by a femtosecond laser pulse," JETP Lett. **87**, 423–427 (2008).
46. S. I. Ashitkov, N. A. Inogamov, V. V. Zhakhovskii, Y. N. Emirov, M. B. Agranat, I. I. Oleinik, S. I. Anisimov, and V. E. Fortov, "Formation of nanocavities in the surface layer of an aluminum target irradiated by a femtosecond laser pulse," JETP Lett. **95**, 176–181 (2012).
47. J.-M. Savolainen, M. S. Christensen, and P. Balling, "Material swelling as the first step in the ablation of metals by ultrashort laser pulses," Phys. Rev. B **84**, 193410 (2011).
48. C. Wu, M. S. Christensen, J.-M. Savolainen, P. Balling, and L. V. Zhigilei, "Generation of subsurface voids and a nanocrystalline surface layer in femtosecond laser irradiation of a single-crystal Ag target," Phys. Rev. B **91**, 035413 (2015).
49. D. A. Papaconstantopoulos, *Handbook of the Band Structure of Elemental Solids: From Z=1 To Z=112* (Springer, 2016).
50. S. Gorbunov, N. Medvedev, P. Terekhin, and A. Volkov, "Electron-lattice coupling after high-energy deposition in aluminum," Nucl. Instruments Methods Phys. Res. Sect. B: Beam Interactions with Mater. Atoms **354**, 220–225 (2015).
51. C. Kittel, *Introduction to Solid State Physics* (Wiley, 1996).
52. L. Jiang and H.-l. Tsai, "Improved two-temperature model and its application in ultrashort laser heating of metal films," J. Heat Transf. **127**, 1167 (2005).
53. N. Ashcroft and N. Mermin, *Solid State Physics*, HRW international editions (Holt, Rinehart and Winston, 1976).
54. Z. Lin, L. V. Zhigilei, and V. Celli, "Electron-phonon coupling and electron heat capacity of metals under conditions of strong electron-phonon nonequilibrium," Phys. Rev. B **77**, 075133 (2008).
55. S. I. Anisimov and B. Rethfeld, "Theory of ultrashort laser pulse interaction with a metal," Proc. SPIE **3093**, 192–203 (1997).
56. C. Y. Ho, R. W. Powell, and P. E. Liley, "Thermal conductivity of the elements," J. Phys. Chem. Ref. Data **1**, 279–421 (1972).

Optics EXPRESS

57. D. L. Windt, "IMD-software for modeling the optical properties of multilayer films," Comput. Phys. **12**, 360 (1998).
58. R. Ramji Rao and A. Ramanand, "Lattice dynamics, thermal expansion, and bulk modulus of ruthenium," J. Low Temp. Phys. **27**, 837–850 (1977).